Supplementary Information for

Discovery of Polarized Twin Walls in a Halide Perovskite

Weilun Li[1], Qimu Yuan[2], Michael B. Johnston[2], Joanne Etheridge[1,3,4*]

[1]School of Physics and Astronomy, Monash University, Victoria, 3800, Australia

[2]Department of Physics, University of Oxford, Oxford OX1 3PU, United Kingdom

[3]Monash Centre for Electron Microscopy, Monash University, Victoria, 3800, Australia

[4]Department of Materials Science and Engineering, Monash University, Victoria, 3800, Australia

*e-mail: joanne.etheridge@monash.edu

This file includes:

Supplementary Note 1-5

Figure S1-S16

References

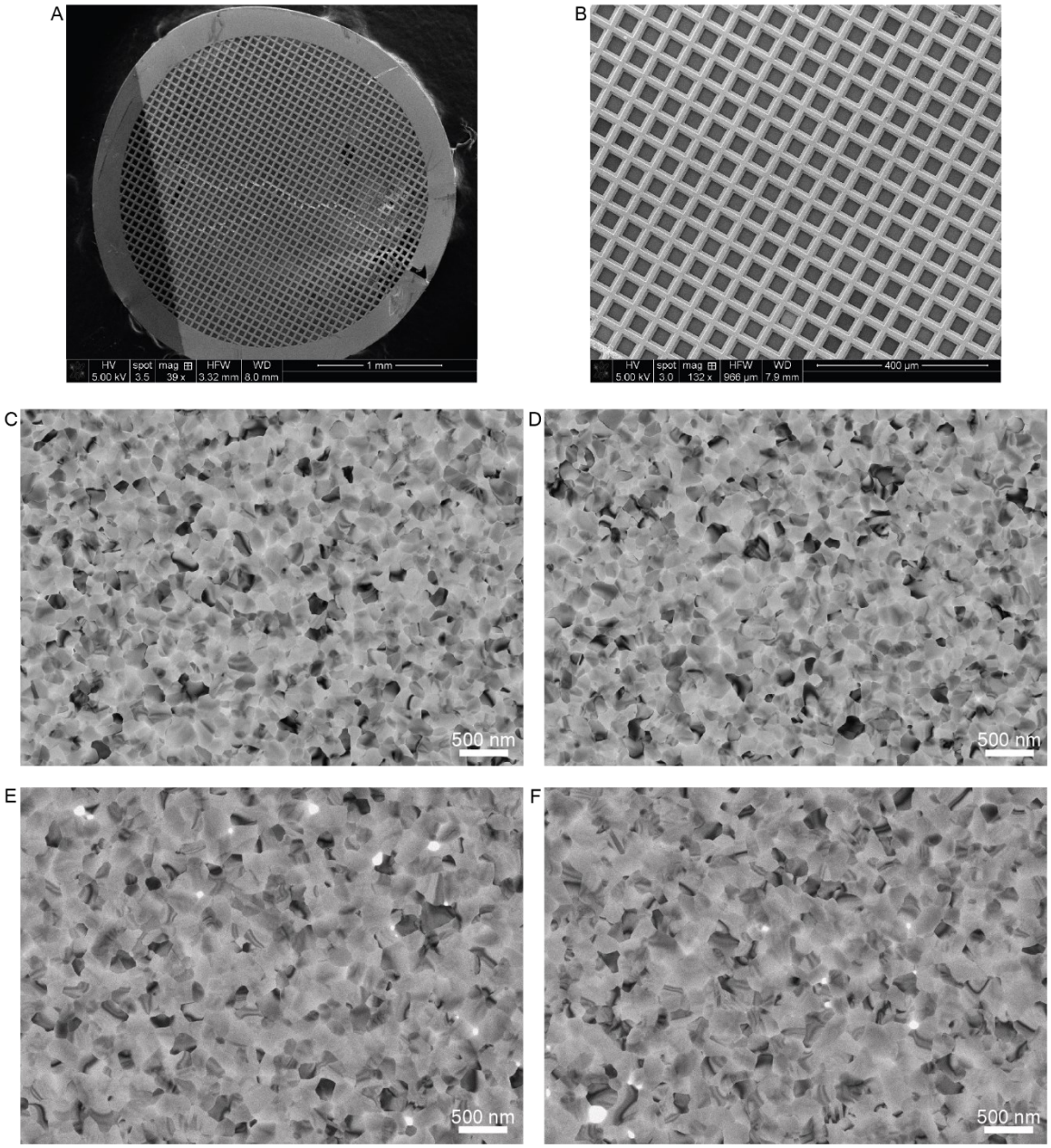


Fig. S1. Overview SEM and HR-TEM images show the homogeneity of $CsPbI_3$ thin films prepared by vapor-deposition. (A, B) Representative SEM images of a typical deposited thin film on carbon-coated TEM Cu grid. **(C)** Specimen 1, mesh 1. **(D)** Specimen 1, mesh 2. **(E)** Specimen 2, mesh 1. **(F)** Specimen 2, mesh 2.

Supplementary Note 1: Phase determination

An experimental diffraction pattern was acquired along the [001] zone axis and compared with simulated electron diffraction patterns to check the γ-phase assignment and estimate the thin-film thickness. Electron diffraction patterns are acutely sensitive to the specimen's space group and thickness due to the very strong interaction of the electron with the crystal's potential and consequent multiple scattering. Electron scattering calculations were executed using the multi-slice algorithm[1] within the abTEM software program[2].

As shown in **Fig. S2**, the experimental pattern agrees best with the simulation for a thickness of 35 nm, consistent with the thickness of 35 nm measured by the quartz crystal microbalances during film deposition. The residual mismatch arises, at least in part, from the slight mis-tilt of the experimental crystal, as crystal tilting was not performed during the experiments to minimize electron dose, and the absence of inelastic scattering in the simulations.

The lattice parameter a and b were measured directly from the diffraction pattern acquired along the [001] zone axis. The measured values (a=0.863±0.037 nm and b=0.884±0.039 nm) agree, within the experimental uncertainties (set primarily by the diffraction pattern pixel size), with the published values obtained by XRD refinement of γ-$CsPbI_3$ films for solar cell devices[3] (ICSD-21955, a=0.86464 nm and b=0.88182 nm) and single-crystal γ-$CsPbI_3$ (a=0.85783(8) nm and b=8.8637(8) nm). In the later XRD results in **Fig. S15**, the (110) peak position at 14.4° for both 35 nm and 200 nm films is also consistent with the literature for γ-$CsPbI_3$ films, including our previously prepared γ-$CsPbI_3$ thick films at 500 nm using the same vapor-deposited method[4,5]. This indicates the absence of significant lattice parameter variations in the thin film relative to bulk γ-$CsPbI_3$.

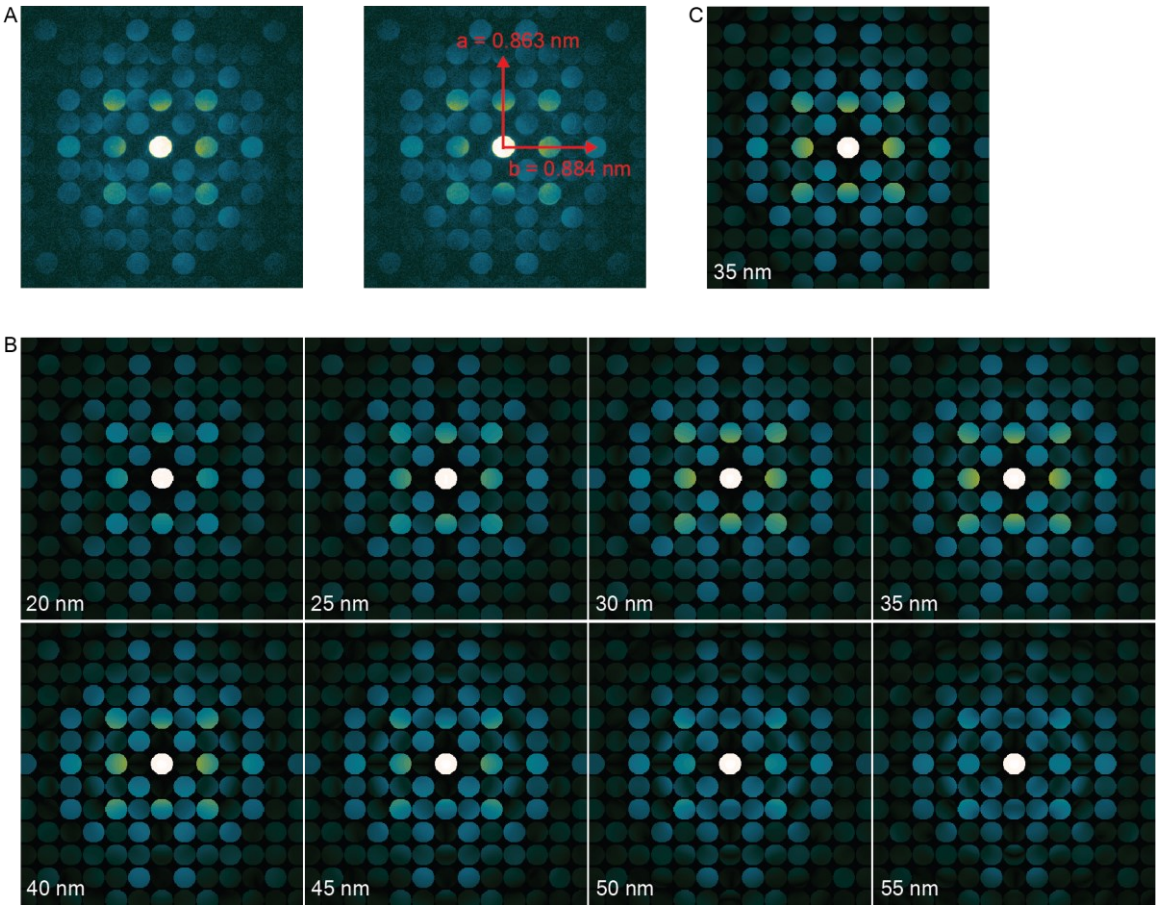


Fig. S2. Diffraction patterns of $CsPbI_3$. (A) Experimental diffraction pattern acquired from a $CsPbI_3$ grain oriented along the [001] zone axis. **(B)** Simulated diffraction patterns of

orthorhombic γ-$CsPbI_3$ (space group *Pbnm*) along the [001] zone axis, for specimen thicknesses ranging from 20 to 55 nm. **(C)** The simulated pattern at 35 nm thickness is repeated for easier comparison with **(A)**.

In **Fig. S3**, we simulate diffraction patterns for common crystal phases of $CsPbI_3$. These patterns can be compared with the experimental diffraction patterns in **Fig. S2** and **Fig. S13**. The diffraction patterns for both zone axes, [001] and [110], are only consistent with the gamma phase (space group *Pbnm*), in agreement with the phase determination based on the atomic-resolution images in **Fig. 1**.

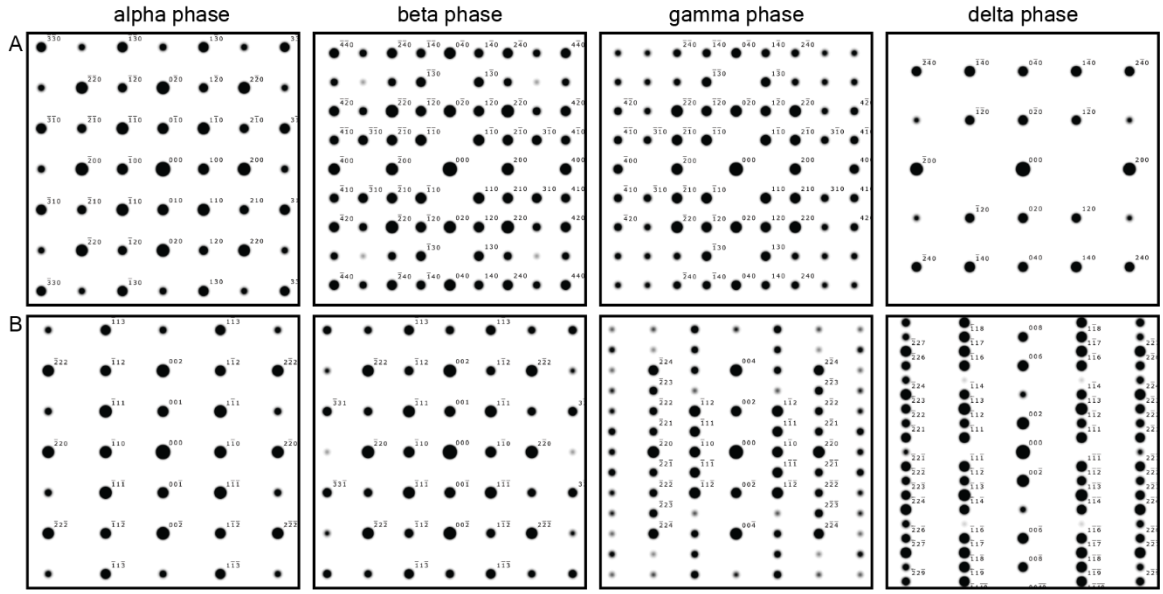


Fig. S3. Simulated diffraction patterns of $CsPbI_3$ polymorphs, along the: (A) [001] zone axis and **(B)** [110] zone axis. Structure files are from the ICSD crystallography database: alpha phase (ICSD-139391), beta phase (ICSD-149865), gamma phase (ICSD-21955), delta phase (ICSD-27979).

Supplementary Note 2: Quantitative measurements from STEM-ADF images

Along the [110] zone axis, out-of-phase octahedral tilts project along the viewing direction, producing elliptically shaped intensity maxima associated with the Pb/I and I columns. To minimize systematic errors in quantitative analyses from these distortions, off-center displacement of Pb were measured relative to the neighboring Cs sites.

To minimize total electron dose and preserve the intrinsic structural integrity of this beam-sensitive material, all images were acquired immediately, as-found, without any tilting of the crystal or other adjustments. Slight deviations from exact zone axis and local bending in the polycrystalline film cause minor variations in the atom displacement maps, particularly where elliptical shapes of atomic columns are most pronounced (**Fig. 1J**, **Fig. S4E**).

Due to slight mistilt of the specimens, the projected Pb/I atomic columns appear with different elliptic orientations, which introduces a varying fitting error between alternating columns. This artefact can break the expected mirror symmetry of neighboring Pb/I position in the displacement analysis. However, the magnitude of this background fitting error (~ 10 pm, as seen in **Fig. 1J**) is substantially smaller than the measured polar displacements at the {110} twin wall (~35 pm in **Fig. 3C**), confirming that the observed polarization is real and not an artefact of image fitting.

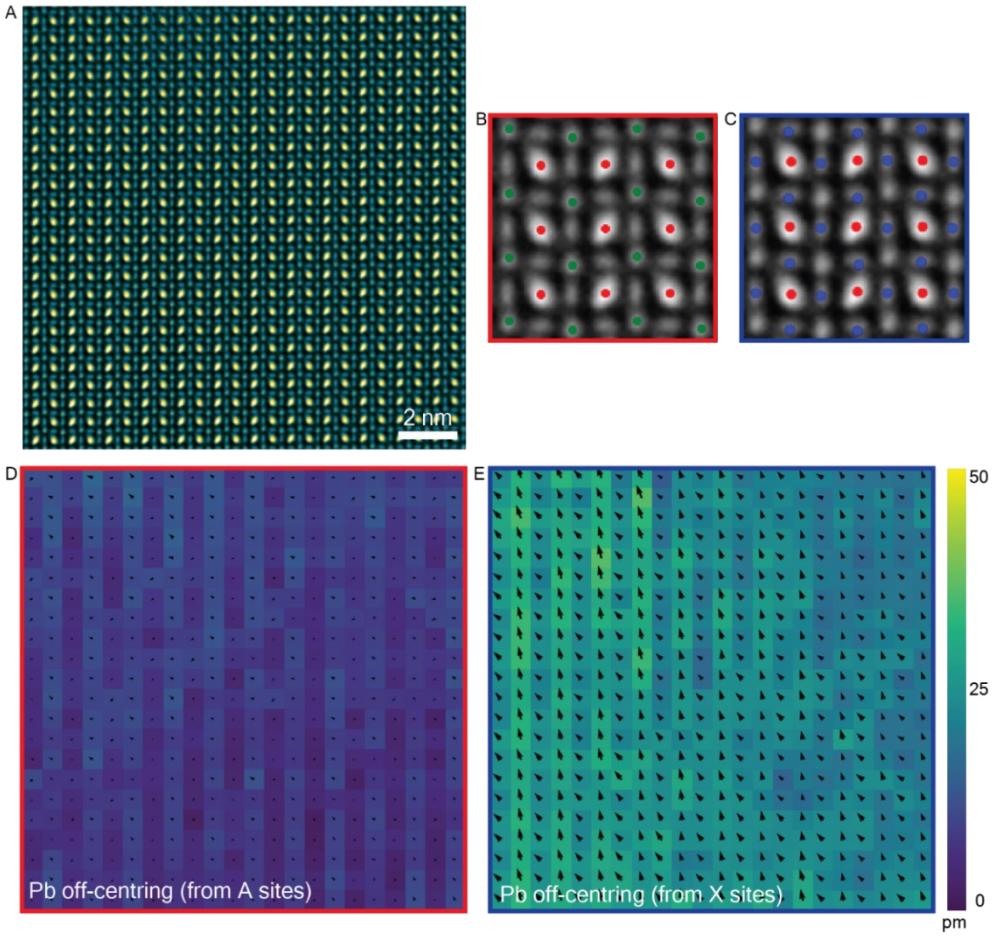


Fig. S4. Quantitative measurements of off-center displacements of Pb atoms in $CsPbI_3$. **(A)** Atomic resolution STEM-ADF image of $CsPbI_3$ acquired along the [110] zone axis. **(B, D)** Maps of Pb off-centering by fitting the positions of Pb/I columns (red) relative to the surrounding Cs columns (green). **(C, E)** Maps of Pb off-centering by fitting the positions of Pb/I columns (red) relative to the surrounding I columns (blue).

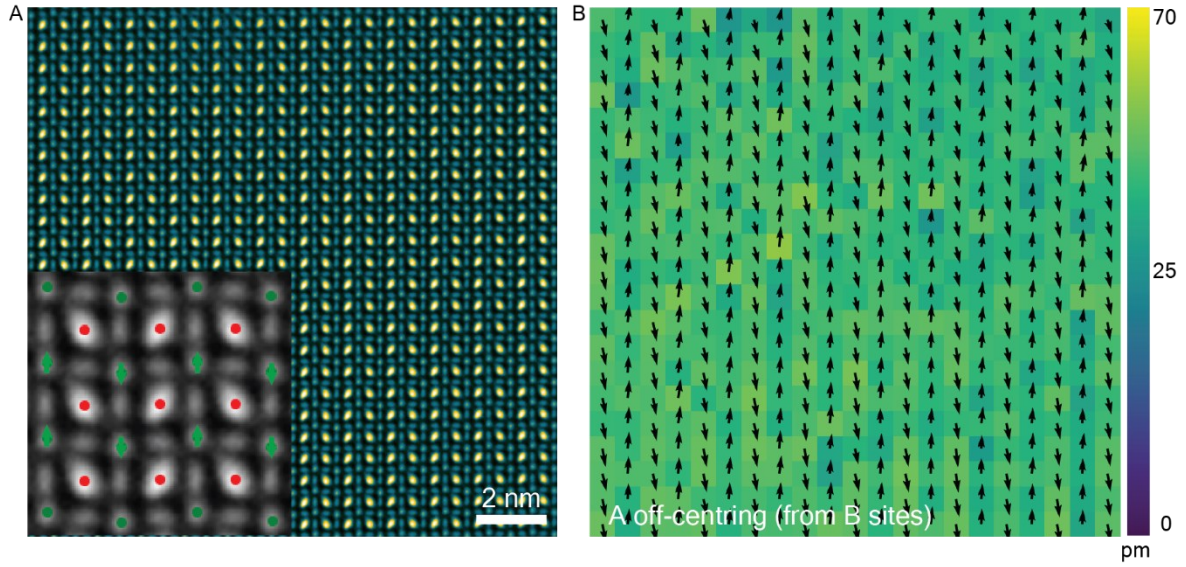


Fig. S5. Quantitative measurement of off-center displacements of Cs relative to four neighboring Pb/I columns. (A) Atomic-resolution STEM-ADF image of a $CsPbI_3$ grain viewed along the [110] zone axis. **(B)** Cs off-centering map revealing the characteristic antipolar displacement of Cs columns.

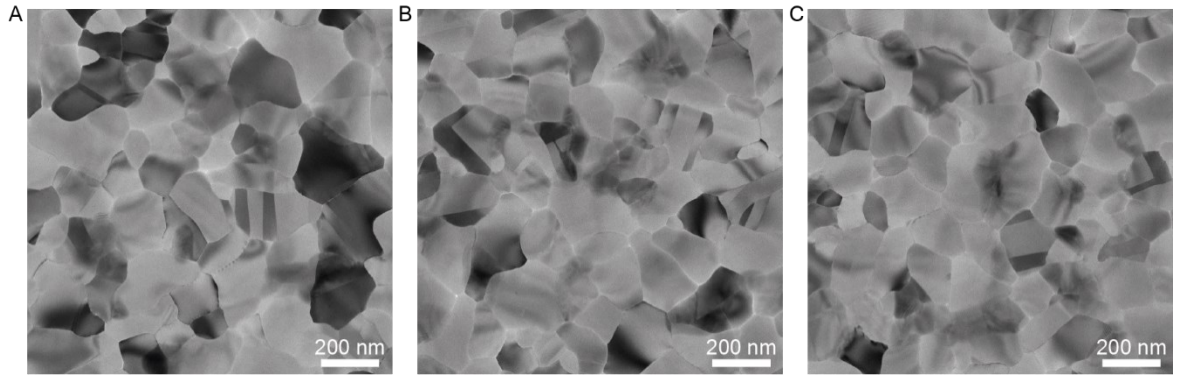


Fig. S6. HR-TEM images of twins in $CsPbI_3$ thin films prepared by vapor-deposition at nominal 35 nm thickness.

Metal halide perovskites are known to be highly sensitive to electron beam damage, particularly at defect sites such as twin walls[6]. To reliably characterize the crystallographic nature of these domains, we first need be sure the features we examine are not induced by beam damage. We therefore adopted a dose-fractionation strategy for data acquisition. For the image shown in **Fig. 2C**, 150 ultra-low-dose images were recorded at 2 e^-/A^2 per frame and subsequently aligned and summed. The structural integrity and beam stability of twin walls in $CsPbI_3$ were assessed by inspecting the full dose-series. As shown in **Fig. S7**, the domain structures are already visible in the first frame (total dose: 2 e^-/A^2), and the twin walls remain stable under further illumination (**Fig. S7(D)).** This confirms that the observed features are intrinsic to the material rather than beam-induced artifacts.

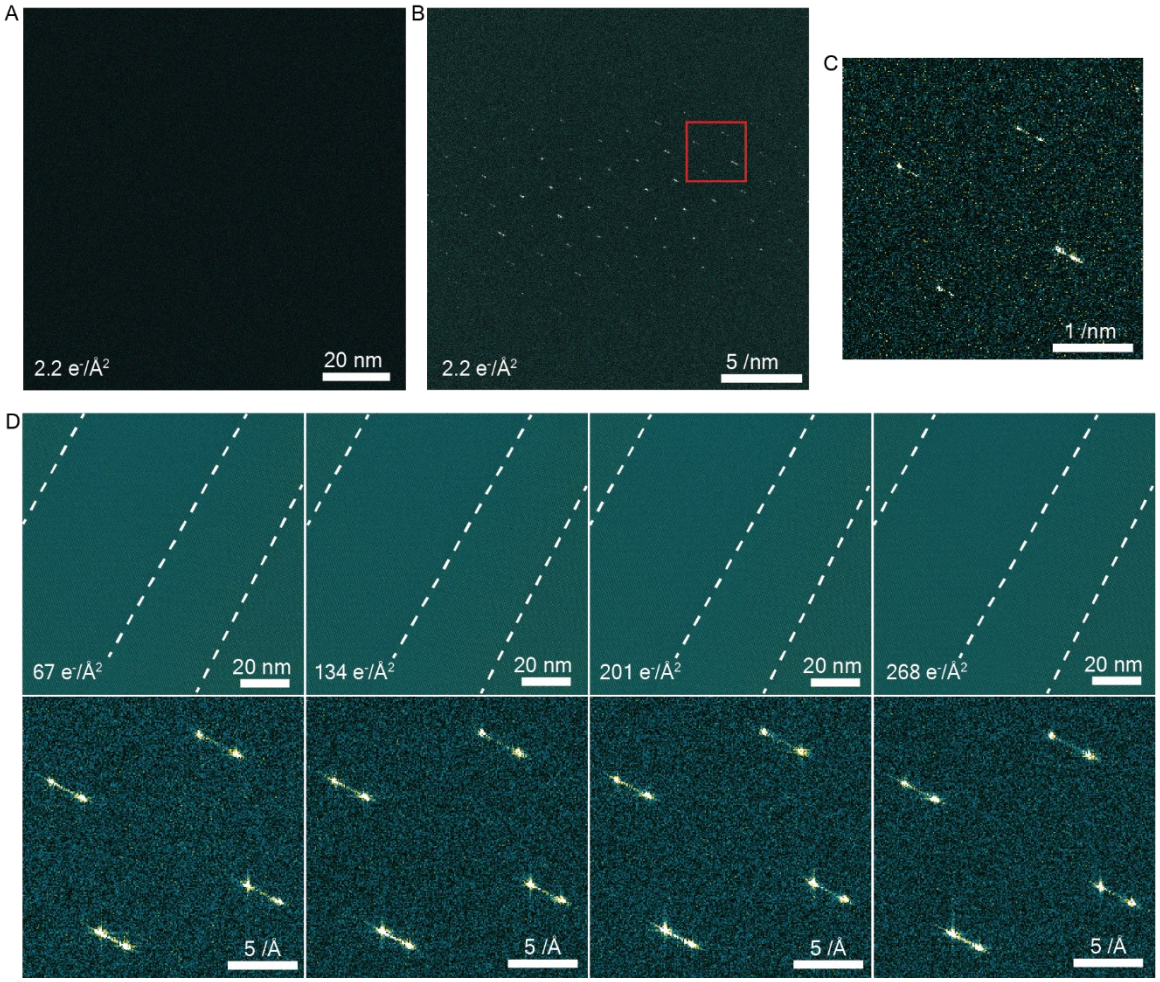


Fig. S7. Ultralow-dose HR-TEM images of $CsPbI_3$ thin films (same dataset as in Fig. 2C). **(A)** HR-TEM image of a representative grain viewed along the [001] zone axis with a total dose at 2 e^-/A^2. **(B)** Fourier Transform of **(A)**. **(C)** Enlarged view of the region highlighted in the red box in **(B)**. **(D)** Dose-series images of the same region and their corresponding Fourier Transform.

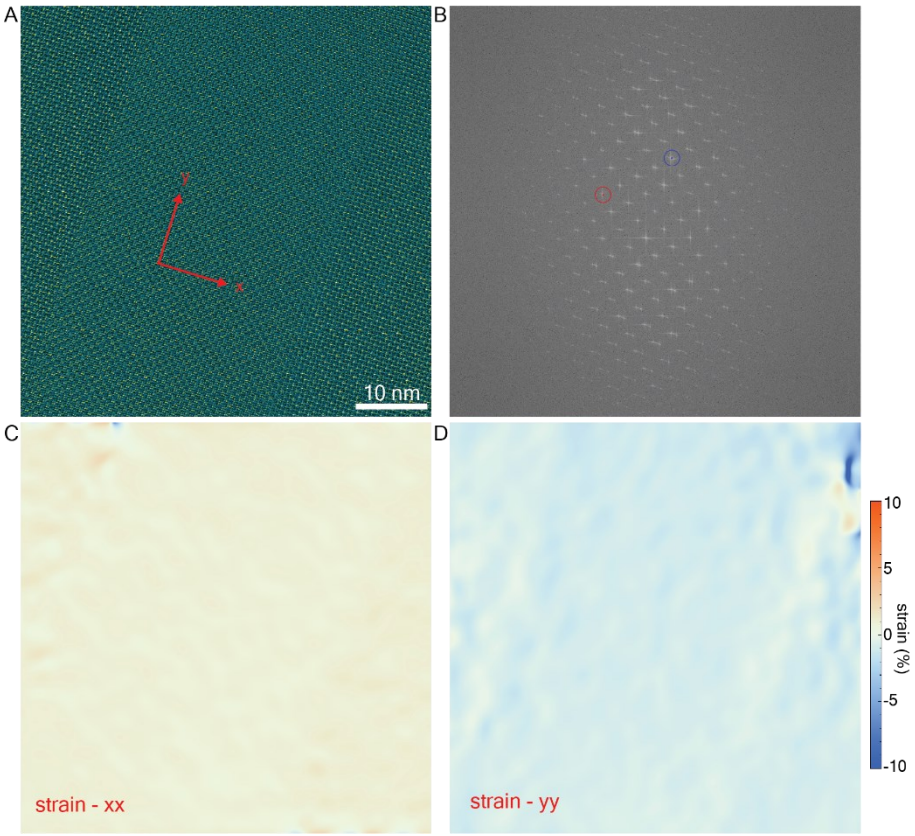


Fig. S8. Strain mapping of the selected region. **(A)** STEM image of the analyzed region. **(B)** Corresponding FFT, with the reflections used for strain mapping circled. **(C)** Strain map along the *x* direction. **(D)** Strain map along the *y* direction.

Supplementary Note 3: Possible image artefacts

Background subtraction was applied to the measured line profiles to remove systematic offsets arising from residual crystal mis-tilt across the image field of view (which is near-impossible to avoid due to the challenge of not orienting the crystal under electron illumination to minimize dose) (**Fig. S9**). The background was estimated by averaging the Pb displacement in regions away from the twin walls. After subtraction, small negative values may appear because the mis-tilt background is not perfectly uniform across the image, as shown for example in **Fig. S12**. Nevertheless, the Pb displacement at the {110} twin wall is significantly larger than the background variation, confirming that the observed polar displacement is not an artefact of residual mis-tilt.

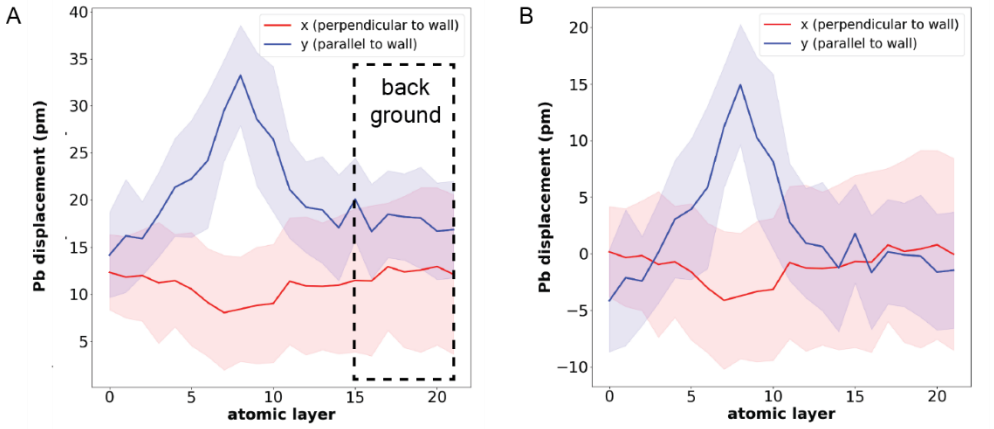


Fig. S9. Background subtraction of the systematic mis-tilt across the twin wall region. (A) Raw line plot. The region marked is considered as background. **(B)** background subtracted line plot.

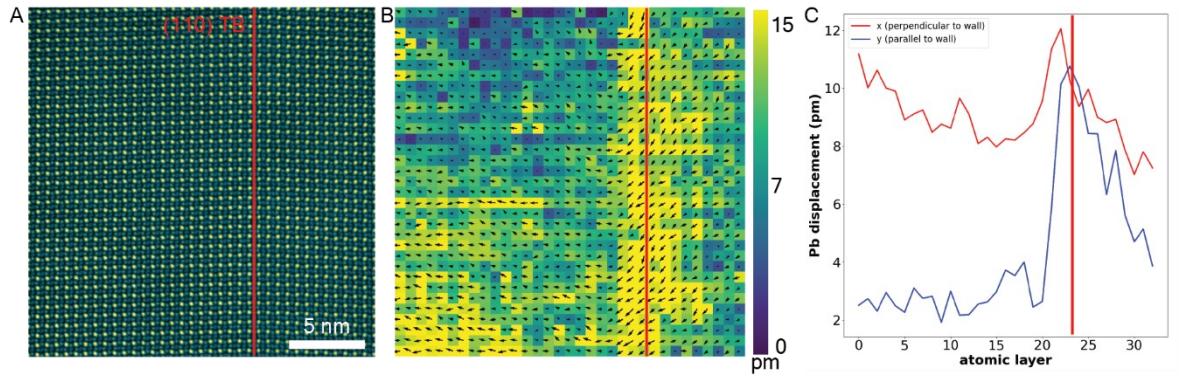


Fig. S10. Quantitative analysis of off-center displacement of Pb atoms at a {110}-type twin wall from a grain that is slightly mis-tilted away from the [001] zone axis (i.e., a small tilt perpendicular to the wall, corresponding to the horizontal direction in the image). (A) Atomic-resolution STEM-ADF image of a [001]-oriented grain containing a (110) twin wall. **(B)** Map of Pb/I column off-centering related to the geometric center of the four surrounding I columns, as illustrated in the insert. Vectors represent the direction and magnitude of Pb atom displacements. **(C)** Components of the Pb atom displacement resolved parallel and perpendicular to the twin wall, obtained by averaging the displacement map in **(B)**. Red lines indicate the position of the twin wall.

Metal halide perovskite, including all-inorganic $CsPbI_3$, are well known to be electron-beam sensitive, whereas quantitative analysis of atom positions requires sufficient signal-to-noise ratio (SNR) and sampling. It is therefore necessary to carefully balance image quality against the risk of beam-induced damage. In this study, we acquired a STEM-ADF image series of 20 frames up to a significant total dose of ~$3x10^4$ e/$Å^2$. The dose was not increased further as this value is close to the reported damage threshold for all-inorganic Cs-based halide perovskites[7].

For the quantitative analysis in **Fig. 3**, all 20 frames were integrated to maximize the SNR. To assess possible beam damage effects and the stability of the measured displacement, we separately integrated frames 1-10 and 10-20 and compared the resulting polarization maps in **Fig. S11**. Both integrated images show localized Pb polarization at the {110} twin wall, with consistent magnitude and spatial distribution in the vector maps. The slightly broader peak in **Fig. S11F** may indicate a subtle beam-induced structural variation, but the persistence of the localized Pb polarization in both frame ranges confirms that the measured polar distortion is reproducible under the applied low-dose imaging conditions.

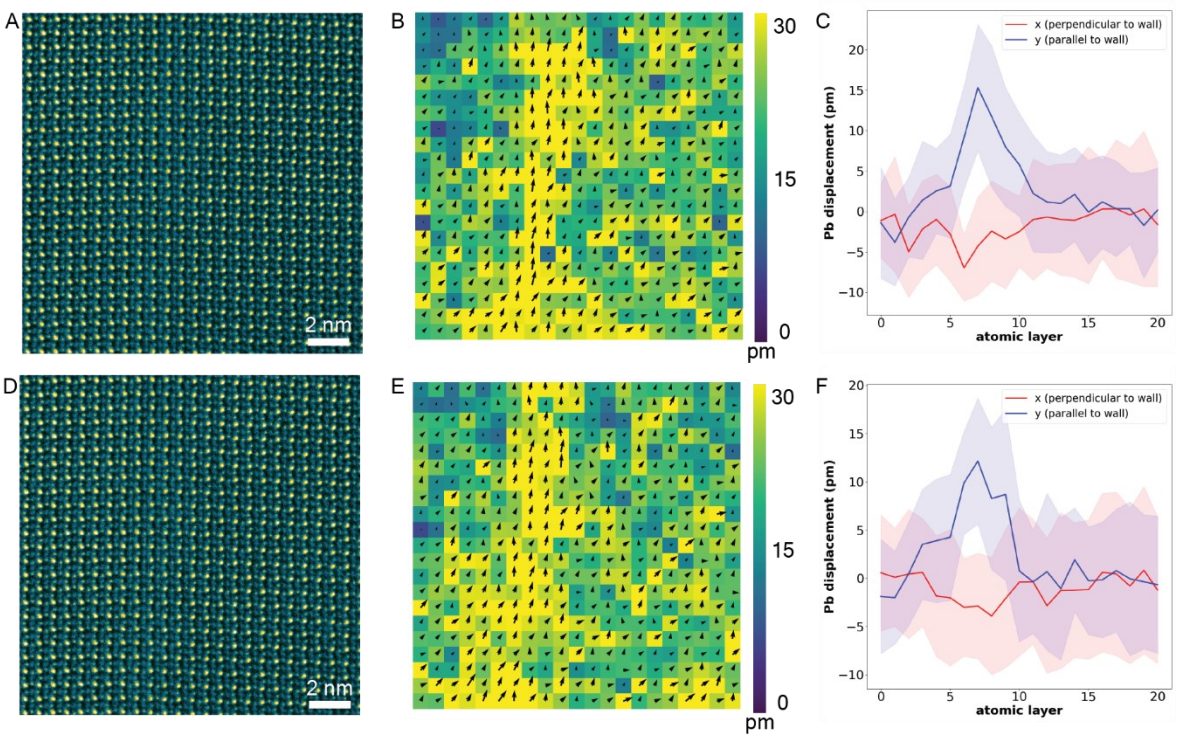


Fig. S11. Dose series analysis of local polarization at the {110} twin wall. (A) First image obtained by integrating STEM-ADF image frames 1-10 in the dose series **(B)** Map of Pb/I column off-center displacements relative to the geometric center of the four surrounding I columns. Vectors represent the direction and magnitude of Pb off-center displacements. **(C)** Components of the Pb displacement vector resolved parallel and perpendicular to the twin wall, obtained by averaging the displacement map in **(B)**. **(D-F)** Corresponding analysis of the second image obtained by integrating frames 11-20 in dose series.

Supplementary Note 4: 4D-STEM measurements

Measuring Centre-of-Mass (CoM) in STEM has been proposed as an effective method for measuring electric fields based on simplified models of electron scattering. However, in the present 35 nm thick specimen, complicated dynamical diffraction effects make quantitative CoM interpretation unfeasible. In addition, residual crystal mis-orientation can dominate the CoM contrast, as shown in **Fig. S12B**.

As an alternative approach to highlight polarity at the twin wall, we selected the region closest to the zone axis and analyzed the intensity variation between Friedel-pair reflections in the diffraction patterns. Unlike XRD, in electron diffraction, Friedel's Law does not hold due to the strength of the electron interaction. In other words, Friedel-pairs are non-equivalent in polar structures. Because of residual mis-tilt, non-equivalent Friedel-pair intensities are still observed away from the twin wall, for example at P1 and P3. However, at the twin wall (P2), the intensity difference between the 220 and $\overline{2}\overline{2}0$ reflections increase significantly, indicating a localized polar symmetry component parallel to the wall (**Fig. S12G**). In contrast, no comparable intensity variations are observed for the Freidel-pair reflections sensitive to the direction perpendicular to the wall (**Fig. S12H**).

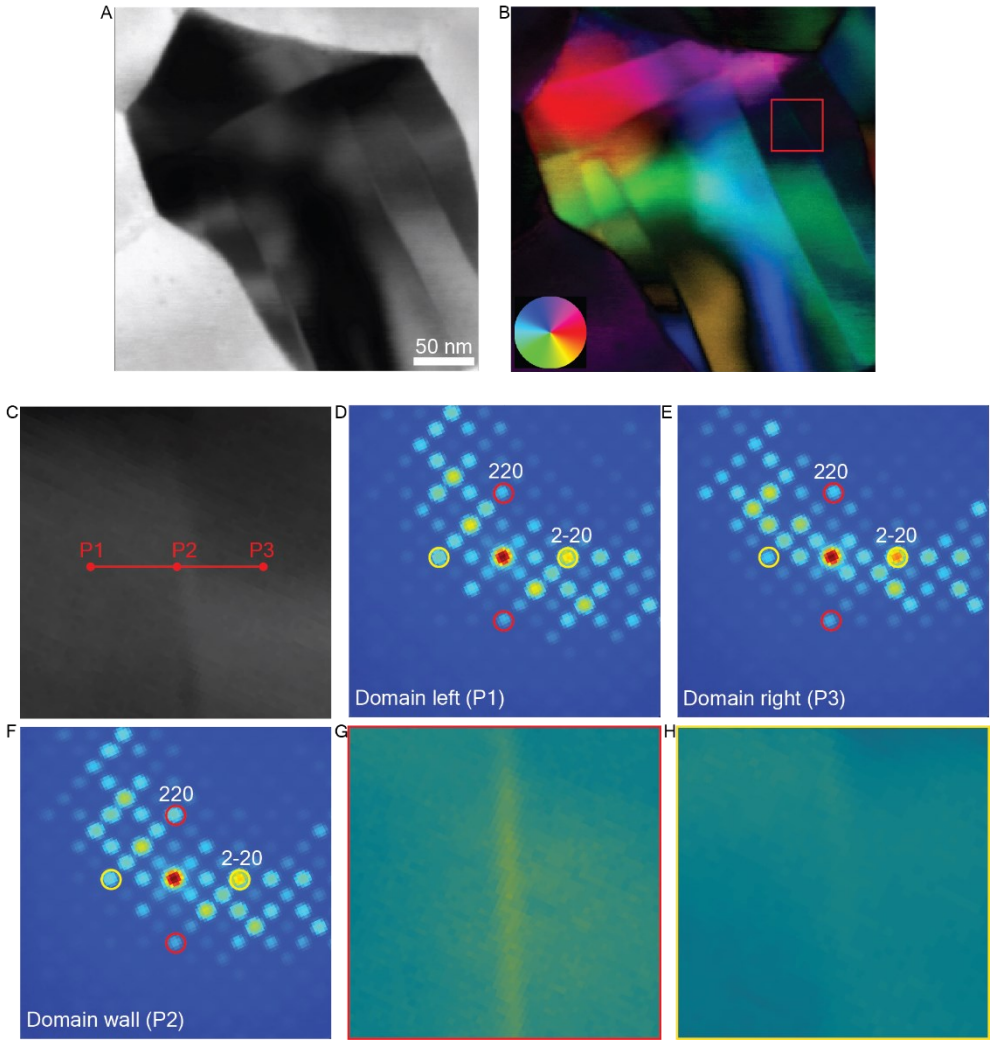


Fig. S12. Friedel pair comparison at twin wall. (A) $CsPbI_3$ grain images near the [001] zone axis using 4D-STEM. **(B)** Variation in orientation. **(C)** region closest to the zone axis as highlighted in **(B)**. **(D-F)** Diffraction patterns extracted from points P1-P3, as indicated in **(C)**. **(G)** Variation of the intensity difference between the 220 and $\overline{2}\overline{2}0$ reflections: Δ(I-220 – I-$\overline{2}\overline{2}0$). **(H)** Variation of the intensity difference between the $\bar{2}20$ and $2\bar{2}0$ reflections: Δ(I-$\bar{2}20$ – I-$2\bar{2}0$).

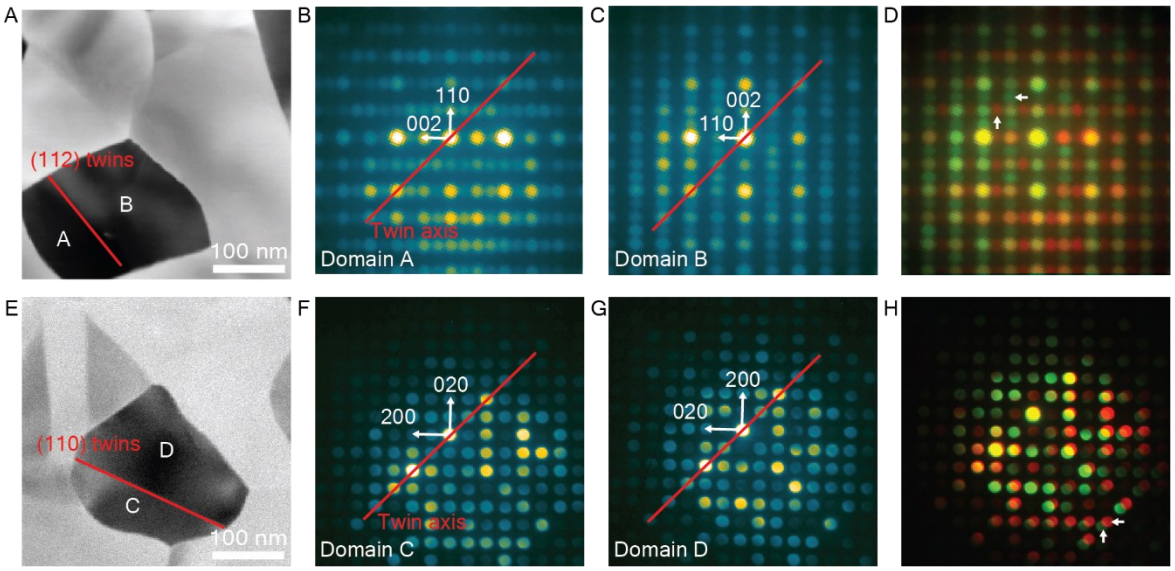


Fig. S13. 4D-STEM of {112} and {110} twin walls in $CsPbI_3$. (A) Image of a [110]-oriented grain generated by integrating all pixel signals within each diffraction pattern of the acquired 4D-STEM dataset. **(B)** Averaged diffraction pattern from domain A. **(C)** Averaged diffraction from domain B. **(D)** Overlay of the two diffraction patterns, with **(B)** shown in red and **(C)** in green. **(E)** Image of a [001]-oriented grain generated by integrating all pixel signals within each diffraction pattern of the acquired 4D-STEM dataset. **(F)** Averaged diffraction pattern from domain C. **(G)** Averaged diffraction pattern from domain D. **(H)** Overlay of the two diffraction patterns, with **(F)** shown in red and **(G)** in green.

Supplementary Note 5: Comparison between thin and thick $CsPbI_3$ films

The 35 nm films used for atomic-resolution TEM were prepared using our previously optimized vapor co-deposition protocol[5]. To compare these TEM-optimized specimens with thicker films, we also prepared 200 nm films on z-cut quartz and measured both corresponding PL and XRD (**Figs. S14-S16**). The 35 and 200 nm films show similar PL emission peaks and XRD patterns dominated by γ-$CsPbI_3$ diffraction peaks, indicating that both the structural phase and the optical properties are comparable across the two thicknesses. Both XRD results also show a weak CsI secondary-phase reflection, consistent with the CsI-rich precursor flux condition that was deliberately used during deposition.

In **Fig. S16**, because the films are strongly textured, relative peak intensities and the visibility of weaker reflections are sensitive to preferred orientation and normalization and should not be interpreted quantitatively as phase fractions. The predominant γ-$CsPbI_3$ reflections remain at the same positions after storage, and no new strong reflections indicative of an obvious phase transformation are resolved. We therefore interpret these data as consistent with retention of the predominant γ-phase over the storage period, rather than as proof of unchanged phase fractions. However, variations are observed in the peak intensities near 28°, corresponding both to CsI and the 004 peak of $CsPbI_3$. These changes may indicate minor degradation, potentially associated with the CsI secondary phase, and $CsPbI_3$ grains whose orientations deviate from the dominant <110> texture of the film.

Importantly, the XRD and PL measurements on the 200 nm films are ensemble-averaged and do not resolve the local twin-wall structure. Atomic-resolution TEM measurements of the polar distortion require thin specimens and hence were only performed on the 35 nm specimens. We therefore have not demonstrated experimentally that polarized twin walls persist in the 200 nm films, this remains a hypothesis. However, first-principles calculations predict polar ferroelastic twin walls in periodic models of $CsPbI_3$, which provides a theoretical basis for expecting that the polar twin walls will also occur in thick specimens.

In the reported $CsPbBr_3$ study[8], the material consisted of approximately 5 nm quantum dots at freezing temperatures whose surface was strongly modified by organic ligands. By contrast, $CsPbBr_3$ in bulk and thin-film form adopts a centrosymmetric, non-polar structure at room temperature, similar to $CsPbI_3$[9,10]. The polarization mechanism in the reported $CsPbBr_3$ quantum dots[8] is therefore special, plausibly associated with size, surface, ligands, boundary conditions and temperature, rather than simply the substitution of Br and I. Moreover, the reported polarization in $CsPbBr_3$ quantum dots at 0.25 μC cm^{-2} is more than an order of magnitude smaller than the 4.35 μC cm^{-2} estimated here for the ferroelastic twin walls.

The polarization observed in our study is instead associated with the local symmetry breaking induced at the ferroelastic twin walls. Polar twin walls have been predicted theoretically in $CaTiO_3$[11], $SrTiO_3$[12] and $CsPbI_3$[13], providing a well-established microscopic theoretical framework for this phenomenon. What has remained lacking is direct experimental evidence in beam-sensitive $CsPbI_3$, owing to the difficulty of preparing suitable specimens and resolving the wall structure by atomic-resolution TEM.

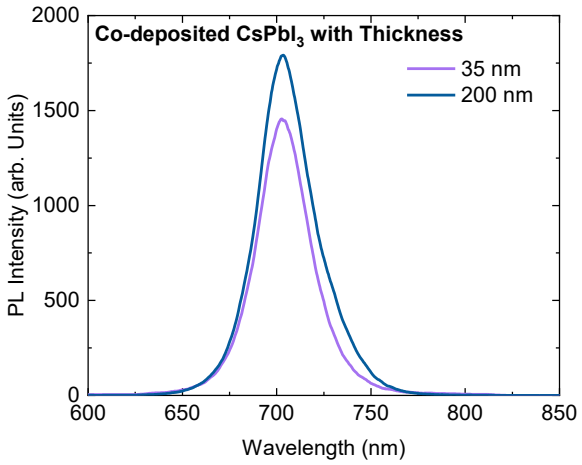


Fig. S14. Unnormalized PL spectra of thin 35 nm and thick 200 nm $CsPbI_3$ co-deposited on z-cut quartz substrates (our standard substrate for optical-based characterizations). PL spectra demonstrate that thinner the sample can be easily reproduced to a much thicker layer.

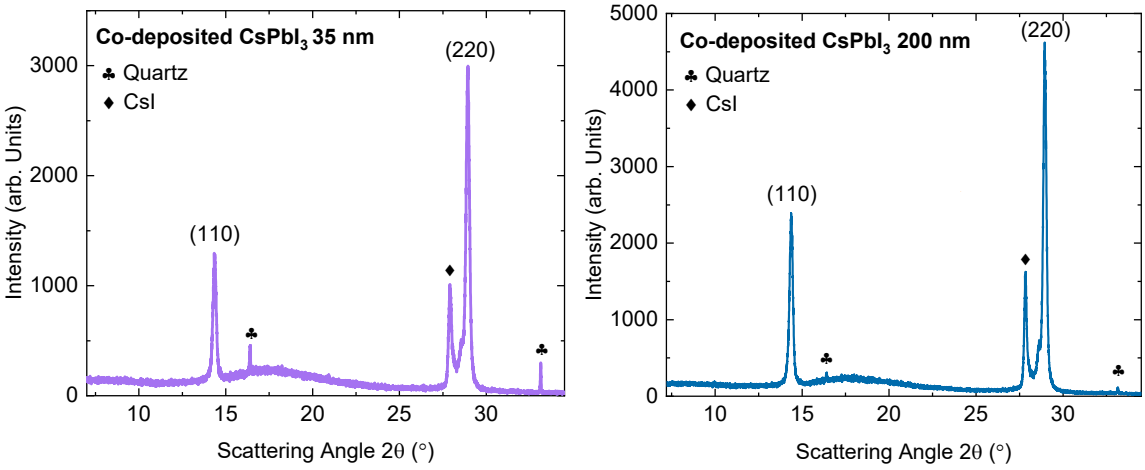


Fig. S15. Unnormalized XRD spectra of both 35 nm-thick and 200-nm thick films on z-cut quartz substrates. XRD spectra demonstrate (1) <110> orientation is preferred, well-correlated with the STEM results; (2) presence of a CsI (001) diffraction peak near 27.5°, which is highly consistent with our nominal precursor flux ratio of ($CsI:PbI_2$) of 1.25:1 employed in co-depositions. Furthermore, these XRD patterns are in excellent agreement with reports from other vapor deposited gamma-phase $CsPbI_3$[14,15].

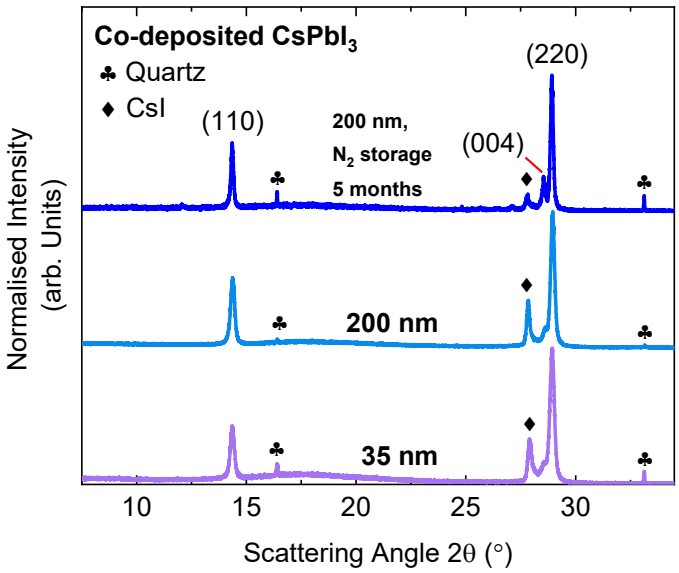


Fig. S16. Normalized XRD spectra of co-deposited $CsPbI_3$ on z-cut quartz substrates. We further analyzed stability-related data from storing the 200 nm-thickness sample in N_2 for approximately 5 months. Although an additional but suppressed (004) diffraction peak is present after extended storage, the presence of this peak is still expected for γ-$CsPbI_3$. This representative measurement indicates that our vapor co-deposited γ-$CsPbI_3$ is mostly phase-stable. Further stability studies, involving heating samples at elevated temperature of 85 ºC can be found in our previous work[5].

References

1. Goodman, P. & Moodie, A. F. Acta Crystallographica Section A - March 1974 - Goodman - Numerical evaluations of N-beam wave functions in electron.pdf. *Found. Crystallogr.* **30**, 280–290 (1974).

2. Madsen, J. & Susi, T. The abTEM code: transmission electron microscopy from first principles. *Open Res. Eur.* **1**, 24 (2021).

3. Zhao, B. *et al.* Thermodynamically stable orthorhombic γ-CsPbI3 thin films for high performance photovoltaics. *J. Am. Chem. Soc.* **140**, 11716–11725 (2018).

4. Sutton, R. J. *et al.* Cubic or Orthorhombic? Revealing the Crystal Structure of Metastable Black-Phase CsPbI3 by Theory and Experiment. *ACS Energy Lett.* **3**, 1787–1794 (2018).

5. Li, W. *et al.* Ruddlesden–Popper Defects Act as a Free Surface: Role in Formation and Photophysical Properties of CsPbI3. *Adv. Mater.* **2501788**, 1–13 (2025).

6. Rothmann, M. U. *et al.* Direct observation of intrinsic twin domains in tetragonal CH3NH3PbI3. *Nat. Commun.* **8**, 6–13 (2017).

7. Zhou, X. G. *et al.* Probing the Electron Beam-Induced Structural Evolution of Halide Perovskite Thin Films by Scanning Transmission Electron Microscopy. *J. Phys. Chem. C* **125**, 10786–10794 (2021).

8. Li, X. *et al.* Evidence for Ferroelectricity of All-Inorganic Perovskite CsPbBr3 Quantum Dots. *J. Am. Chem. Soc.* **142**, 3316–3320 (2020).

9. Bari, M., Bokov, A. A., Leach, G. W. & Ye, Z. G. Ferroelastic Domains and Effects of Spontaneous Strain in Lead Halide Perovskite CsPbBr3. *Chem. Mater.* **35**, 6659–6670 (2023).

10. Zhang, X., Wang, F., Zhang, B. Bin, Zha, G. & Jie, W. Ferroelastic Domains in a CsPbBr3 Single Crystal and Their Phase Transition Characteristics: An in Situ TEM Study. *Cryst. Growth Des.* **20**, 4585–4592 (2020).

11. Lu, G., Catalan, G. & Salje, E. K. H. Antiferroelectric switching inside ferroelastic domain walls. *Phys. Rev. Lett.* **135**, 206103 (2025).

12. He, R. *et al.* Ferroelastic Twin-Wall-Mediated Ferroelectriclike Behavior and Bulk Photovoltaic Effect in SrTiO3. *Phys. Rev. Lett.* **132**, 176801 (2024).

13. Warwick, A. R., Íniguez, J., Haynes, P. D. & Bristowe, N. C. First-Principles Study of Ferroelastic Twins in Halide Perovskites. *J. Phys. Chem. Lett.* **10**, 1416–1421 (2019).

14. Zhang, Z. *et al.* Efficient Thermally Evaporated -CsPbI3 Perovskite Solar Cells.pdf. *Adv. Energy Mater.* **11**, 2100299 (2021).

15. Becker, P. *et al.* Temperature Synthesis of Stable -CsPbI3 Perovskite Layers for Solar Cells.pdf. *Adv. Energy Mater.* **9**, 1900555 (2019).